ADVANCING EARTH AND SPACE SCIENCES

Geophysical Research Letters®

Butterfly Distributions of Energetic Electrons Driven by Ducted and Nonducted Chorus Waves

Yangguang Ke[1,2] ⓘ, Xinliang Gao[1,2] ⓘ, Quanming Lu[1,2] ⓘ, Xueyi Wang[3] ⓘ, and Rui Chen[1,2] ⓘ

[1]CAS Key Lab of Geospace Environment, School of Earth and Space Sciences, University of Science and Technology of China, Hefei, China, [2]CAS Center for Excellence in Comparative Planetology, Hefei, China, [3]Physics Department, Auburn University, Auburn, AL, USA

Abstract Bursts of electron butterfly distributions at 10s keV correlated with chorus waves are frequently observed in the Earth's magnetosphere. Strictly ducted (parallel) upper-band chorus waves are proposed to cause them by nonlinear cyclotron trapping. However, chorus waves in these events are probably nonducted or not strictly ducted. In this study, test-particle simulations are conducted to investigate electron scattering driven by ducted (quasi-parallel) and nonducted upper-band chorus waves. Simulation results show butterfly distributions of 10s keV electrons can be created by both ducted and nonducted upper-band chorus waves in seconds. Ducted upper-band chorus waves cause these butterfly distributions mainly by accelerating electrons due to cyclotron phase trapping. However, nonducted waves tend to decelerate electrons to form these butterfly distributions via cyclotron phase bunching. Our study provides new insights into the formation mechanisms of electron butterfly distributions and demonstrates the importance of nonlinear interactions in the Earth's magnetosphere.

Plain Language Summary The pitch angle distributions (PADs) of energetic electrons in the Earth's outer radiation belt are often modified by wave-particle interactions. In recent years, the bursts of butterfly PADs of 10s keV electrons correlated with upper-band chorus waves are frequently observed. By assuming these chorus waves are strictly ducted (parallel) along the geomagnetic field, previous test-particle simulations suggest nonlinear cyclotron trapping is mainly responsible for the bursts of these butterfly PADs. In this study, test-particle simulations in combination with two-dimensional (2-D) electron magnetohydrodynamics simulations are carried out to investigate how ducted (quasi-parallel) and nonducted upper-band chorus waves modify the electron PADs. Simulation results show that ducted chorus waves cause the bursts of butterfly PADs of 10s keV electrons by cyclotron phase trapping, consistent with previous simulation studies on strictly ducted chorus waves. However, nonducted chorus waves cause those by cyclotron phase bunching. Our study provides new insights into the formation mechanisms of the electron butterfly distributions.

1. Introduction

The pitch angle distributions (PADs) of energetic electrons in the Earth's outer radiation belt are highly dynamic and exhibit three major types: 90° peaked, flattop, and butterfly distributions (Fritz et al., 2003; Gannon et al., 2007; Gu et al., 2011; Horne et al., 2003; Meredith et al., 2000; Zhao et al., 2014). Among them, butterfly distributions, characterized by local flux minima around 90° pitch angle, have long been an attractive object of study, since their formation is associated with various physical processes (e.g., Fritz et al., 2003; Ni et al., 2015, 2016; West et al., 1973). Currently, several formation mechanisms of the butterfly PADs have been proposed: (a) drift shell splitting (Selesnick & Blake, 2002; Sibeck et al., 1987), (b) magnetopause shadowing (West et al., 1972, 1973), (c) outward radial diffusion and adiabatic transports (Lyons, 1977; Su et al., 2010), (d) modulation by localized background magnetic field perturbation (Artemyev et al., 2015; Xiong et al., 2017), and (e) wave-particle interactions (e.g., Horne et al., 2007; Xiao et al., 2015). Electron butterfly PADs are usually observed at nightside with $L = 5$–9 (L is the L-shell) during quiet time, which are mostly attributed to drift shell splitting and magnetopause shadowing in an asymmetric geomagnetic field (e.g., Selesnick & Blake, 2002; West et al., 1973). During geomagnetic activities, electron butterfly PADs are observed at all magnetic local time (MLT) within $L = 6$ (Lyons & Williams, 1975; Sibeck et al., 1987), which can be caused by different mechanisms mentioned above.

Drift shell splitting and magnetopause shadowing are theoretically energy independent, which can cause the butterfly PADs of tens of keV to several MeV electrons at larger L-shells (e.g., Fritz et al., 2003; Sibeck et al., 1987). Wave-particle interactions that are energy dependent are also an important contributor to the

formation of electron butterfly PADs especially at lower L-shells (e.g., Horne et al., 2007; J. Li et al., 2016; Xiao et al., 2015). Many previous studies have shown that the butterfly PADs of hundreds of keV to several MeV electrons are usually induced by magnetosonic (MS) waves, plasmaspheric hiss, and chorus waves (e.g., Albert et al., 2016; Hua et al., 2019; J. Li et al., 2014, 2016; Ma et al., 2015; Ni et al., 2017, 2018, 2020; Xiao et al., 2015). In recent years, the bursts (within ∼30 s) of electron butterfly PADs at tens of keV, with high correlations with chorus waves, are frequently observed in the Earth's magnetosphere (Fennell et al., 2014; Kurita et al., 2018; Peng et al., 2022). Observational statistics reveal that more than 80% of these events are upper-band chorus dominated events and these events tend to occur over ∼21-05 MLT at $L = $ ∼4.5–6.5 (Peng et al., 2022). By assuming these chorus waves are strictly ducted (parallel), previous test-particle simulations suggest nonlinear cyclotron trapping is mainly responsible for the bursts of these butterfly PADs (Gan, Li, Ma, Artemyev, & Albert, 2020; Saito et al., 2021). However, chorus waves in these events are probably nonducted or not strictly ducted, since many of these events are observed without a density structure (see Figure S1). Chorus waves can be ducted (quasi-parallel) in a density structure and propagate nearly along the magnetic field lines (e.g., R. Chen et al., 2021; Ke et al., 2021; Liu et al., 2021; Streltsov et al., 2006). However, nonducted chorus waves tend to become oblique-propagating gradually (e.g., Breuillard et al., 2012; Gao, Lu, et al., 2022; Lu et al., 2019) after leaving their equatorial sources (e.g., LeDocq et al., 1998; W. Li et al., 2009; Santolík et al., 2005). The relations between nonducted chorus waves and electron butterfly PADs at tens of keV is less well-known. In this study, test-particle simulations combined with electron magnetohydrodynamics (EMHD) simulations have been used to investigate electron scattering driven by ducted and nonducted upper-band chorus waves. Simulation results show that ducted and nonducted upper-band chorus waves lead to the butterfly PADs of tens of keV electrons through different nonlinear processes.

2. Simulation Model

To model chorus waves in the inner magnetosphere, the geomagnetic field is set as a dipole magnetic field $B_0 = B_{0eq} \frac{\sqrt{1+3\sin^2\lambda}}{\cos^6\lambda}$, where $B_{0eq} \approx 3 \times 10^4$ nT/L^3 and λ is the magnetic latitude. The electron density (in cm^{-3}) in the plasma trough is set based on an empirical model (Carpenter & Anderson, 1992; Denton et al., 2002, 2006),

$$n_e = (n_{eq} + n_d)(\cos\lambda)^{-2a}, \tag{1}$$

$$n_{eq} = n_{e0}L^{-4.5} + \left(1 - e^{-\frac{L-2}{10}}\right), \tag{2}$$

here a is set to 1 and $n_{e0} = 5{,}800 + 300$ MLT ($0 \leq$ MLT < 6). In normal (nonducted) cases, $n_d = 0$. In the presence of a density duct, n_d is given as

$$n_d = \frac{\delta n}{2}\left[1 + \cos\frac{\pi(L-L_0)}{D_L/2}\right], L_0 - D_L/2 \leq L \leq L_0 + D_L/2, \tag{3}$$

where L_0 and D_L are respectively the central location and the radial width of this duct. We perform three simulation cases: a ducted case with $L_0 = 5.5$, $D_L = 0.035$, and $\delta n = -0.1 n_{eq}(L_0)$, and two nonducted cases with different wave source scales. Our simulations are carried out around $L = 5.5$ at MLT $= 0$, which are typical conditions for bursts of electron butterfly PADs based on observational statistics (Peng et al., 2022).

A two-dimensional (2-D) EMHD model (Ke, Gao, et al., 2022) is used to simulate the propagation of upper-band chorus waves. 2-D EMHD simulations are widely used to study the propagation of chorus waves (e.g., Hanzelka & Santolík, 2022; Hosseini et al., 2021; Katoh, 2014). Chorus waves are excited by the energetic electrons injected from the magnetotail and drifting eastward around the Earth, which usually consist of quasi-periodical discrete elements with frequency chirping and a majority of them exhibit rising-tone elements (Burtis & Helliwell, 1969; W. Li et al., 2012; Tsurutani & Smith, 1974). The repetition period of chorus elements is found to be correlated with the drift velocity of energetic electrons (Gao, Chen, et al., 2022; Lu et al., 2021), which has a typical value of ∼0.5 s, and each element lasts from ∼0.1 to 1 s (Shue et al., 2015, 2019; Teng et al., 2017). The transverse source scale of chorus elements is estimated in the range ∼100–800 km (∼0.016–0.126 R_E, R_E is the earth radius) based on multiple-satellite measurements (e.g., Agapitov et al., 2017, 2018; Santolík & Gurnett, 2003; Shen et al., 2019). In our simulations, parallel upper-band chorus waves with a repetition period
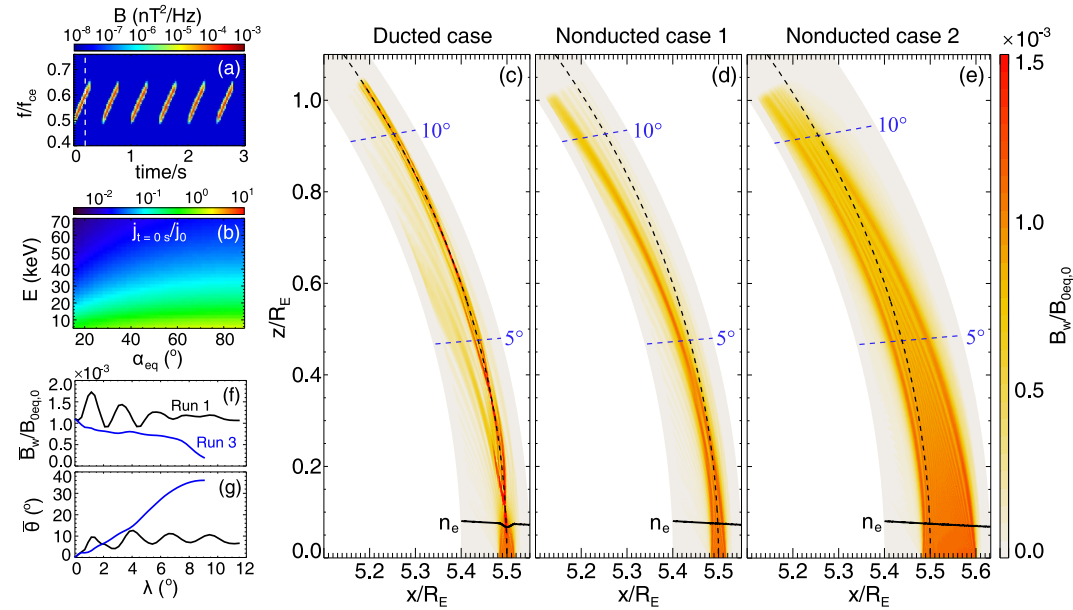
Figure 1. (a) The frequency-time spectrogram of upper-band chorus waves launched from the magnetic equator and (b) the initial electron flux distribution at the magnetic equator in our simulations. (c)–(e) The spatial profiles of magnetic field amplitudes of chorus waves at $t = 0.2$ s in three simulation cases. (f), (g) The averaged amplitude $\overline{B}_w$ and wave normal angle $\overline{\theta}$ of these chorus waves at $f/f_{ce} = 0.55$–0.6 along $L_0 = 5.5$ in Ducted case and Nonducted Case 2.

$T_{RP} = 0.5$ s and a typical element duration $T_D = 0.3$ s are launched from an equatorial source region. For each chorus element, its frequency f rises evenly from $0.5f_{ce}$ to $0.65f_{ce}$ and its amplitude remains constant $B_{w0} = 0.0011B_{0eq,0} = 0.2$ nT in the middle phase, but rises (drops) in the initial (end) phase $T_{ini}(T_{end}) = 0.1T_D$ ($B_{0eq,0}$ is $B_{0eq}(L_0)$ and f_{ce} is the equatorial electron gyrofrequency at L_0). The wave spectra are shown in Figure 1a. The chorus source scale is set as $\Delta L = 0.042$ ($L = 5.479$–5.521) in Ducted case and Nonducted Case 1, and $3\Delta L = 0.126$ ($L = 5.479$–5.605) in Nonducted Case 2. Moreover, the wave amplitudes decrease from B_{w0} to 0 in the inner and outer edges (with a width $\delta_L = 0.0042$) of each source region. The simulation domain within $\lambda \approx -15°$–$15°$, has $L = 5.4$–5.55 in Ducted case and Nonducted Case 1, and $L = 5.4$–5.63 in Nonducted Case 2. The L-shell width in Case 2 is 1.533 times that in Case 1. Absorbing boundary conditions are applied for waves. Assuming the wave fields are confined to $|\lambda| < 15°$ is reasonable for upper-band chorus waves according to satellite statistics (e.g., Meredith et al., 2009; Teng et al., 2019). The simulation grid numbers in parallel and perpendicular directions are $N_{\parallel} = 16,000$ and $N_{\perp} = 1,000$ (or 1,533) for Ducted case and Nonducted Case 1 (or Nonducted Case 2).

Test-particle simulations are used in combination with the 2-D EMHD simulations. Initially, test electrons are located at the equator at $L_0 = 5.5$. They are uniformly distributed in the energy E from 2 to 90 keV with $\Delta E = 2$ keV, the equatorial pitch angle α_{eq} from 5° to 89° with $\Delta \alpha_{eq} = 2°$ (the loss cone ~3°), and the gyroangle φ from 0° to 354° with $\Delta \varphi = 6°$. A particle weight is given to each test electron according to the initial electron flux distribution assumed as

$$j(E, \alpha_{eq}) = j_0 \left(\frac{E}{E_0} \right)^{-p} \sin \alpha_{eq}, \tag{4}$$

where j_0 is the differential flux at $E_0 = 10$ keV and $\alpha_{eq} = 90°$. The index p is set as 1 and 2 at energies less and greater than E_0, respectively. The initial electron flux distribution is shown in Figure 1b. The similar power law distributions of energetic electrons are widely used in previous works (e.g., Bortnik et al., 2011; L. Chen et al., 2012; Saito & Miyoshi, 2022). The simulation time step is 1.5771×10^{-6} s and the total simulation time is 3 s.
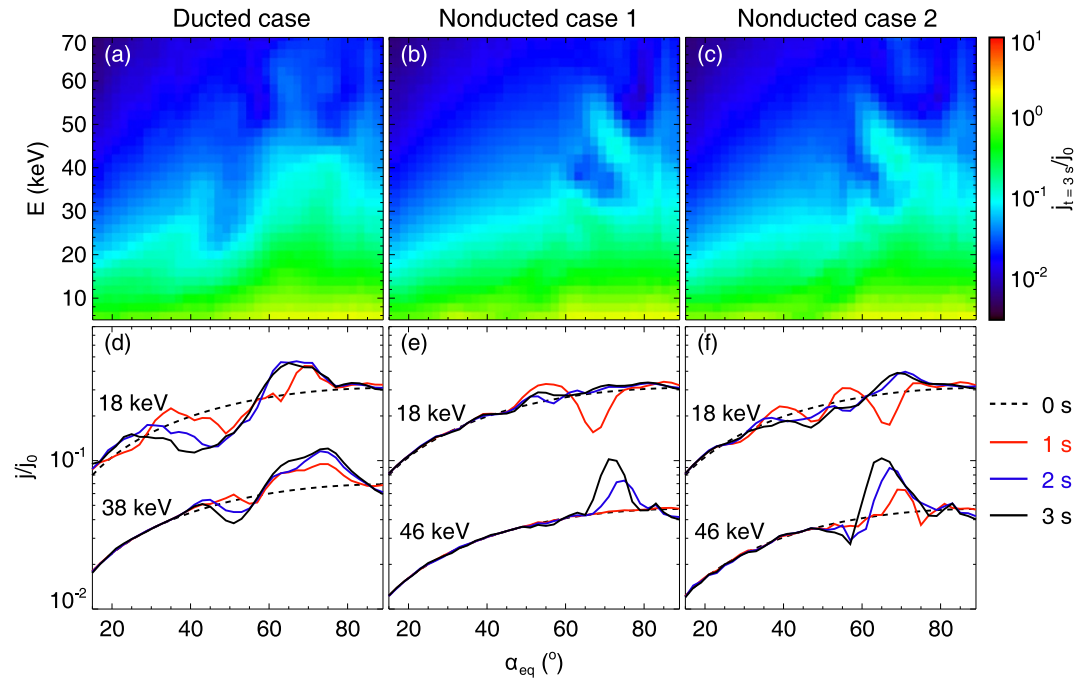
Figure 2. (a–c) The electron flux distributions as a function of the equatorial pitch angle and the energy at $t = 3$ s and (d–f) the pitch angle distributions of electrons at two energy channels at $t = 0$, 1, 2, and 3 s in three simulation cases.

3. Simulation Results

Figure 1 shows an overview of ducted and nonducted propagations of the chorus waves in our EMHD simulations. Figures 1c–1e show the spatial profiles of magnetic field amplitudes of upper-band chorus waves at $t = 0.2$ s (marked by the dashed line in Figure 1a) in three simulation cases. Figure 1c illustrates that upper-band chorus waves propagate nearly along the magnetic field lines in a density duct of 10% density reduction. Obviously, these upper-band chorus waves are ducted by the depleted duct, consistent with previous studies (e.g., Liu et al., 2021; Smith et al., 1960). Without a density duct, upper-band chorus waves gradually deviate from the magnetic field lines across the wave source region (simply called source field lines) during their propagation. Most of these nonducted waves completely deviate from source field lines at $|\lambda| < 5°$ in Nonducted Case 1 and at $|\lambda| < 10°$ in Nonducted Case 2 (Figures 1d and 1e). The averaged amplitude $\overline{B}_w$ and wave normal angle $\overline{\theta}$ of these chorus waves at $f/f_{ce} = 0.55$–0.6 along $L_0 = 5.5$ are estimated (in Ducted case and Nonducted Case 2) and shown in Figures 1f and 1g, respectively. In Ducted case, $\overline{B}_w$ and $\overline{\theta}$ of these chorus waves fluctuate around $0.0011B_{0eq,0}$ and $8°$ at $|\lambda| \leq 11.5°$, respectively. Both $\overline{B}_w$ and $\overline{\theta}$ are not shown at $|\lambda| > 11.5°$, since these waves decay sharply due to absorbing boundary conditions. In Nonducted Case 2, $\overline{B}_w/B_{0eq,0}$ of these chorus waves decreases from 0.0011 to 0.0006 within $|\lambda| \leq 7.5°$, and then drops quickly to 0.0002 within $|\lambda| = 7.5°$–$9°$, since more nonducted waves deviate from source field lines at higher latitudes. Besides, $\overline{\theta}$ of these nonducted waves increases rapidly with the latitude, reaching up to $36°$ at $|\lambda| = 9°$.

Figure 2 shows the simulation results of the flux distributions of energetic electrons projected on the equatorial plane. Figures 2a–2c present the electron flux distributions at $t = 3$ s in three simulation cases. Compared to the initial flux distributions (Figure 1b), the flux distributions at $t = 3$ s are greatly modified by the chorus waves, which are clearly different in ducted and nonducted cases. In Ducted case, chorus waves cause significant flux decreases and increases at $\alpha_{eq} \sim 40°$–$60°$ and $\alpha_{eq} \sim 60°$–$80°$, respectively. In Nonducted cases, chorus waves cause both significant flux increases and decreases at $\alpha_{eq} \sim 60°$–$80°$. Besides, the significant flux increases in Nonducted cases occur at higher energies than those in Ducted case. The greatest relative flux increase $(j_{t=3s}/j_{t=0s})_{max}$ appears at $E \sim 38$ keV in Ducted case and $E \sim 46$ keV in Nonducted cases. Figures 2d–2f show the temporal variation of electron PADs at two energy channels: $E = 18$ keV and $E = 38$ (or 46) keV in three cases. These PADs at $E = 38$ (or 46) keV in Ducted case (or Nonducted cases) gradually become butterfly PADs over
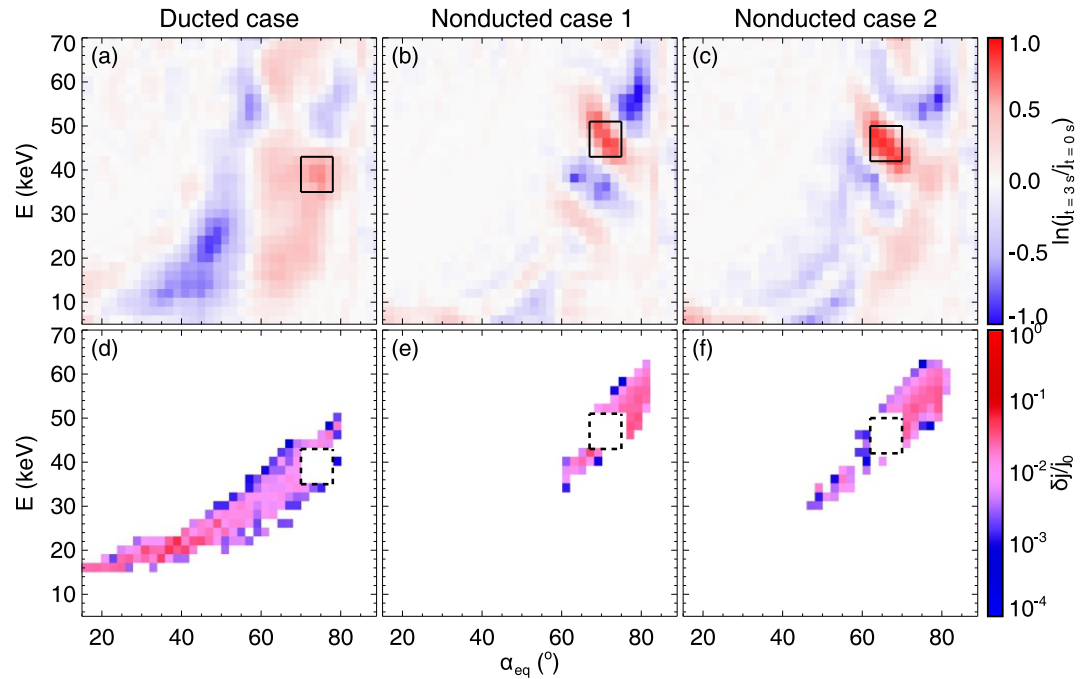
Figure 3. (a–c) The ratios of the electron fluxes at $t = 3$ s and $t = 0$ s in three simulation cases. A box with $\Delta E = 8$ keV and $\Delta \alpha_{eq} = 8°$ is located in a region with the largest averaged flux ratio in each panel. (d–f) The initial flux distributions of the electrons scattered into the box (at $t = 3$ s) in three simulation cases.

time. These PADs at $E = 18$ keV become butterfly PADs only in Ducted case. We identify a butterfly PAD based on two criteria. The first is similar to that of Ni et al. (2016): $j(90°) < \beta \times j_{avg}(\alpha: 90°)$, where $j(90°)$ is the electron flux at $\alpha_{eq} = 90°$, $j_{avg}(\alpha: 90°)$ is the averaged electron flux over the pitch angle range between α and $90°$, α is selected from $45°$ to $85°$ to determine the maximum value of $j_{avg}(\alpha: 90°)$, and the index β is set as 0.95. This criterion is to identify an electron PAD with a minimum flux at $90°$. The second is $j_{max} \geq \eta \times j(90°)$, where j_{max} is the maximum flux at $\alpha_{eq} = 0–90°$ and the threshold η is set as 1.5. This criterion is to exclude those PADs with slight flux variations, like the PADs at $E = 18$ keV in Nonducted Case 1 at $t \geq 2$ s (Figure 2e). Based on the criteria, the energy ranges (widths) of the butterfly PADs are estimated as 16–44 keV (28 keV), 36–58 keV (22 keV), and 36–54 keV (18 keV) in Ducted case, Nonducted Case 1, and Nonducted Case 2, respectively.

The ratios of the electron fluxes at $t = 3$ s and $t = 0$ s in three simulation cases are shown in Figures 3a–3c, which indicate where the fluxes increase or decrease. In Ducted case, the large flux increases appear at $E \sim 16–46$ keV and $\alpha_{eq} \sim 60°–80°$, while the evident flux decreases appear at lower energies and pitch angles (Figure 3a). In Nonducted Case 1 and Case 2, the large flux increases occur at $E \sim 38–58$ keV and $\alpha_{eq} \sim 60°–75°$, while the main flux decreases occur at higher energies and pitch angles (Figures 3b and 3c). A box with $\Delta E = 8$ keV and $\Delta \alpha_{eq} = 8°$ is located in a region with the largest averaged flux ratio in each panel of Figure 3. The central location (E, α_{eq}) of this box is (39 keV, 74°) in Ducted case, (47 keV, 71°) in Nonducted Case 1, and (46 keV, 66°) in Nonducted Case 2. Figures 3d–3f show the initial flux distributions of the electrons scattered into the box (at $t = 3$ s) in three cases. In Ducted case, 91% of the scattered electrons are accelerated, and their α_{eq} also increase. Most of them are initially distributed at $E \sim 15–35$ keV and $\alpha_{eq} \sim 15°–70°$. However, 77% (or 84%) of the scattered electrons are decelerated in Nonducted Case 1 (or Case 2), and their α_{eq} also decrease. Most of them are initially distributed at energies up to ~ 63 keV and pitch angles up to $\sim 82°$. Obviously, these electrons scattered into the box are accelerated or decelerated by upper-band chorus waves through the cyclotron resonance rather than the Landau resonance, which causes the opposite variations of E and α_{eq}. In a word, ducted upper-band chorus waves cause these butterfly PADs of 10s keV electrons mainly by accelerating electrons, while nonducted waves do the opposite.

The typical trajectories of an accelerated electron in Ducted case and a decelerated electron in Nonducted Case 2 are presented in Figure 4, which shows the energy E, pitch angle α_{eq}, and parallel velocity $v_{\parallel}$ as functions of the
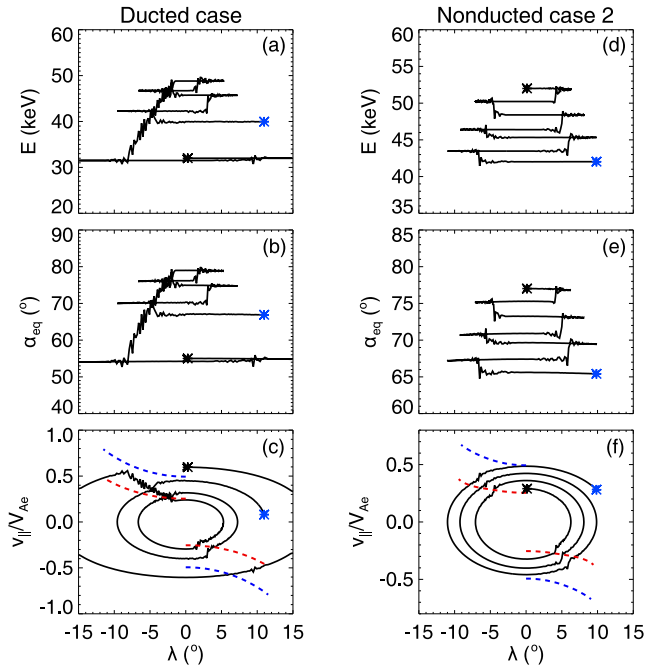
Figure 4. (a–c) The energy E, equatorial pitch angle α_{eq}, and parallel velocity $v_\parallel$ of a typical accelerated electron in Ducted case as functions of the magnetic latitude λ. (d–f) The E, α_{eq}, and $v_\parallel$ of a typical decelerated electron in Nonducted Case 2 as functions of λ. The unit of $v_\parallel$ is $V_{Ae} = B_{0eq,0}/\sqrt{\mu_0 m_e n_{eq}(L_0)}$, where μ_0 is the permeability of vacuum. The blue and red dotted lines mark the cyclotron resonant velocities v_R at $f = 0.5f_{ce}$ and $f = 0.7f_{ce}$. The black and blue asterisks mark the start and end of the trajectories.

magnetic latitude. This electron in Ducted case, with an initial energy of $E \sim 30$ keV, is first accelerated to ~ 50 keV from $\lambda = -8°$ to $\lambda = -2°$, and then undergoes several rapid decelerations at $|\lambda| \leq 5°$, finally reaching 40 keV (Figure 4a). The variation trend of α_{eq} is very similar to that of E for this electron (Figure 4b). The parallel velocity $v_\parallel$ decreases with fluctuating around the cyclotron resonant velocities v_R in the acceleration phase, and increases sharply with intersecting v_R in the rapid deceleration phases (Figure 4c). Obviously, this electron first undergoes nonlinear phase trapping and then potentially experiences phase bunching. This electron in Nonducted Case 2, with an initial energy of $E = 52$ keV, only undergoes several rapid decelerations, like the electron decelerations in Ducted case. It probably experiences several times of phase bunching at $|\lambda| \leq 7°$, and finally drops to 42 keV (Figures 4d–4f).

If an electron is phased trapped, the phase ζ between its perpendicular velocity $\boldsymbol{v}_\perp$ and the wave perpendicular magnetic field $\boldsymbol{B}_{w\perp}$ will change periodically and satisfy $0 < \zeta < 2\pi$. In simulation results, phase trapping of an electron is identified by the criterion: the phase ζ satisfies $0 < \zeta < 2\pi$ for more than five periods. A group of electrons with the same initial E and α_{eq} but uniformly distributed gyrophases are scattered roughly symmetrically by quasilinear scattering, but most of them are scattered to lower E and α_{eq} by phase bunching (e.g., Bortnik et al., 2008). Generally, phase bunching leads to significantly larger energy and pitch angle changes than those caused by quasilinear scattering. We assume such a group of electrons are in a quasilinear scattering period until $|\overline{\Delta E}| > 0.1\sqrt{\overline{(\Delta E - \overline{\Delta E})^2}}$, where ΔE is the energy change of each electron within a half bounce period T_{hb} (Gan, Li, Ma, Albert, et al., 2020). An electron is assumed to be phase bunched if $\Delta E < -|\Delta E|_{\max}$ and $\Delta\alpha_{eq} < -|\Delta\alpha_{eq}|_{max}$ within T_{hb}, where $|\Delta E|_{\max}$ and $|\Delta\alpha_{eq}|_{\max}$ are the maximum energy and pitch angle changes within T_{hb} of all the electrons in

their quasilinear scattering periods. In three simulation cases, $|\Delta E|_{\max}$ and $|\Delta\alpha_{eq}|_{\max}$ are found to be about 1 keV and 1°. For the electrons scattered into the box in Ducted case, 78% of them have experienced phase trapping, and 81% of them have experienced phase bunching. Finally, most of them get accelerated as a result of competition between phase trapping and phase bunching. Besides, 64% of the trapped electrons begin their trapping at $|\lambda| > 9°$. For the electrons scattered into the box in Nonducted Case 1 (or Case 2), 72% (or 86%) of them have experienced phase bunching, but only 22% (or 25%) of them have experienced phase trapping. Finally, most of them get decelerated due to multiple phase bunchings, which mainly occur at $|\lambda| < 5°$.

4. Discussion and Conclusions

In this study, test-particle simulations in combination with 2-D EMHD simulations have been performed to study the scattering of 10s keV electrons driven by ducted and nonducted upper-band chorus waves. Our simulation results suggest ducted waves cause the butterfly PADs of 10s keV electrons mainly by accelerating electrons via cyclotron phase trapping, while nonducted waves cause these butterfly PADs mainly by decelerating electrons via cyclotron phase bunching. We explain the difference based on nonlinear resonant conditions (Bell, 1984, 1986; Tao & Bortnik, 2010). Cyclotron phase trapping is possible under the condition:

$$\omega_t^2/h(z,t) > 1, \tag{5}$$

which are described in Equations 2–4 of Bell (1986). When the chorus waves resonate with an electron of 10s keV at $\alpha_{eq} < \sim 60°$ at $|\lambda| < 10°$, there are

$$\omega_t^2 \approx \omega_{t0}^2 = \frac{q_e k_\parallel v_\perp}{m_e}(B_{w\perp 1} + B_{w\perp 2}), \tag{6}$$

where q_e and m_e are the electron charge and mass, $k_\parallel$ is the parallel wave number, $B_{w\perp1}$ and $B_{w\perp2}$ are two components of the perpendicular wave magnetic field. The inhomogeneity factors $h(z, t)$ at $|\lambda| < 10°$ for ducted and nonducted waves are slightly different, which are mainly related to the inhomogeneity of the background magnetic field $\frac{\partial \Omega_e}{\partial z}$ and the wave frequency chirping rate $\frac{\partial \omega}{\partial t}$. Obviously, the wave magnetic field amplitudes B_w dominate the difference in $\omega_t^2/h(z,t)$ of ducted and nonducted waves. Phase bunching is easy to occur when $\omega_t^2/h(z,t)$ is much greater than 1. Thus, it easily occurs for both ducted and nonducted waves at lower latitudes ($|\lambda| \leq 5°$) because of the smaller $h(z,t)$ due to the smaller $\frac{\partial \Omega_e}{\partial z}$ $\left(\frac{\partial \Omega_e}{\partial z} = 0 \text{ at } \lambda = 0°\right)$. The amplitudes B_w of ducted waves decrease slightly along the magnetic field lines due to the ducted propagation, and easily satisfy $\omega_t^2/h(z, t) > 1$ even at higher latitudes ($|\lambda| > 5°$). Thus, ducted waves trap and accelerate electrons to produce the butterfly PADs. Although phase bunching is also involved in the electron dynamics, the acceleration effect due to phase trapping is dominant. The amplitudes B_w of nonducted waves decrease rapidly along the magnetic field lines due to the nonducted propagation, and hardly satisfy $\omega_t^2/h(z, t) > 1$ at higher latitudes. Thus, nonducted waves mainly decelerate electrons to causes the butterfly PADs, since phase bunching is dominant in the electron dynamics. Besides, we have also performed two simulation cases with the smaller amplitude $B_{w0} = 0.05$ nT (the other parameters are same to those of Ducted case and Nonducted Case 1) and another two simulation cases with L-shell around $L_0 = 6.5$, and the simulation results give the same conclusions.

Nonducted chorus waves potentially accelerate electrons by Landau trapping, which contributes less to the formation of electron butterfly PADs in our simulations. In Ke, Lu, et al. (2022), a lower-band chorus with a constant frequency $f/f_{ce} = 0.4$ and the amplitude $B_{w0} = 0.005B_{0eq,0}$ can form the butterfly PADs of tens of keV electrons by Landau trapping. There are two main reasons for the difference. One reason is that the lower-band chorus almost propagates along the magnetic field line at $|\lambda| < 15°$. Another reason is that the amplitude of the lower-band chorus is much larger. Therefore, the lower-band chorus is easier to satisfy the condition of Landau trapping for tens of keV electrons at large pitch angles.

In the realistic magnetosphere, the magnetic amplitude of nonducted upper-band chorus waves may decrease faster due to Landau damping (Bortnik et al., 2007), which is not included in our EMHD simulations. Thus, nonducted upper-band chorus waves are more likely to form the electron butterfly PADs through phase bunching. However, the observational evidence is still lacking. Kurita et al. (2018) provided an observation event detected by Arase, which indicates the electron butterfly PADs result from acceleration of lower energy electrons. Unfortunately, the plasma density data are absent in the same period. It is not easy to determine whether the electron butterfly PADs observed by Van Allen Probes in previous studies originate from lower or higher energy electrons due to low resolution (Fennell et al., 2014; Peng et al., 2022). Thus, the observational evidence is also required as a future work. The primary conclusions are summarized as follows.

1. Test-particle simulations in combination with 2-D EMHD simulations demonstrate both ducted and nonducted upper-band chorus waves can form significant butterfly distributions of tens of keV electrons within seconds.
2. Ducted upper-band chorus waves tend to cause the butterfly distributions of tens of keV electrons by accelerating electrons via cyclotron phase trapping.
3. Nonducted upper-band chorus waves tend to decelerate electrons to cause the butterfly distributions of tens of keV electrons via cyclotron phase bunching.

Data Availability Statement

Simulation data sets for this research are available at Ke et al. (2024).

References

Agapitov, O., Blum, L. W., Mozer, F. S., Bonnell, J. W., & Wygant, J. (2017). Chorus whistler wave source scales as determined from multipoint Van Allen probe measurements. *Geophysical Research Letters*, *44*(6), 2634–2642. https://doi.org/10.1002/2017GL072701

Agapitov, O., Mourenas, D., Artemyev, A., Mozer, F. S., Bonnell, J. W., Angelopoulos, V., et al. (2018). Spatial extent and temporal correlation of chorus and hiss: Statistical results from multipoint THEMIS observations. *Journal of Geophysical Research: Space Physics*, *123*(10), 8317–8330. https://doi.org/10.1029/2018JA025725

Albert, J. M., Starks, M. J., Horne, R. B., Meredith, N. P., & Glauert, S. A. (2016). Quasi-linear simulations of inner radiation belt electron pitch angle and energy distributions. *Geophysical Research Letters*, *43*(6), 2381–2388. https://doi.org/10.1002/2016GL067938

Artemyev, A. V., Agapitov, O. V., Mozer, F. S., & Spence, H. (2015). Butterfly pitch angle distribution of relativistic electrons in the outer radiation belt: Evidence of nonadiabatic scattering. *Journal of Geophysical Research: Space Physics*, *120*(6), 4279–4297. https://doi.org/10.1002/2014JA020865

Bell, T. F. (1984). The nonlinear gyroresonance interaction between energetic electrons and coherent VLF waves propagating at an arbitrary angle with respect to the Earth's magnetic field. *Journal of Geophysical Research*, *89*(A2), 905–918. https://doi.org/10.1029/JA089iA02p00905

Bell, T. F. (1986). The wave magnetic field amplitude threshold for nonlinear trapping of energetic gyroresonant and Landau resonant electrons by nonducted VLF waves in the magnetosphere. *Journal of Geophysical Research*, *91*(A4), 4365–4379. https://doi.org/10.1029/JA091iA04p04365

Bortnik, J., Chen, L., Li, W., Thorne, R. M., & Horne, R. B. (2011). Modeling the evolution of chorus waves into plasmaspheric hiss. *Journal of Geophysical Research*, *116*(A8), A08221. https://doi.org/10.1029/2011JA016499

Bortnik, J., Thorne, R. M., & Inan, U. S. (2008). Nonlinear interaction of energetic electrons with large amplitude chorus. *Geophysical Research Letters*, *35*(21), L21102. https://doi.org/10.1029/2008GL035500

Bortnik, J., Thorne, R. M., & Meredith, N. P. (2007). Modeling the propagation characteristics of chorus using CRRES suprathermal electron fluxes. *Journal of Geophysical Research*, *112*(A8), A08204. https://doi.org/10.1029/2006JA012237

Breuillard, H., Zaliznyak, Y., Krasnoselskikh, V., Agapitov, O., Artemyev, A., & Rolland, G. (2012). Chorus wave-normal statistics in the Earth's radiation belts from ray tracing technique. *Annales Geophysicae*, *30*(8), 1223–1233. https://doi.org/10.5194/angeo-30-1223-2012

Burtis, W. J., & Helliwell, R. A. (1969). Banded chorus-A new type of VLF radiation observed in the magnetosphere by OGO 1 and OGO 3. *Journal of Geophysical Research*, *74*(11), 3002–3010. https://doi.org/10.1029/JA074i011p03002

Carpenter, D. L., & Anderson, R. R. (1992). An ISEE/whistler model of equatorial electron density in the magnetosphere. *Journal of Geophysical Research*, *97*(A2), 1097–1108. https://doi.org/10.1029/91ja01548

Chen, L., Bortnik, J., Li, W., Thorne, R. M., & Horne, R. B. (2012). Modeling the properties of plasmaspheric hiss: 1. Dependence on chorus wave emission. *Journal of Geophysical Research*, *117*(A5), A05201. https://doi.org/10.1029/2011JA017201

Chen, R., Gao, X., Lu, Q., Chen, L., Tsurutani, B. T., Li, W., et al. (2021). In situ observations of whistler-mode chorus waves guided by density ducts. *Journal of Geophysical Research: Space Physics*, *126*(4), e2020JA028814. https://doi.org/10.1029/2020JA028814

Denton, R. E., Goldstein, J., & Menietti, J. D. (2002). Field line dependence of magnetospheric electron density. *Geophysical Research Letters*, *29*(24), 2205. https://doi.org/10.1029/2002GL015963

Denton, R. E., Takahashi, K., Galkin, I. A., Nsumei, P. A., Huang, X., Reinisch, B. W., et al. (2006). Distribution of density along magnetospheric field lines. *Journal of Geophysical Research*, *111*(A4), A04213. https://doi.org/10.1029/2005JA011414

Fennell, J. F., Roeder, J. L., Kurth, W. S., Henderson, M. G., Larsen, B. A., Hospodarsky, G., et al. (2014). Van Allen Probes observations of direct wave-particle interactions. *Geophysical Research Letters*, *41*(6), 1869–1875. https://doi.org/10.1002/2013GL059165

Fritz, T. A., Alothman, M., Bhattacharjya, J., Matthews, D. L., & Chen, L. (2003). Butterfly pitch angle distributions observed by ISEE-1. *Planetary and Space Science*, *51*(3), 205–219. https://doi.org/10.1016/S0032-0633(02)00202-7

Gan, L., Li, W., Ma, Q., Albert, J. M., Artemyev, A. V., & Bortnik, J. (2020). Nonlinear interactions between radiation belt electrons and chorus waves: Dependence on wave amplitude modulation. *Geophysical Research Letters*, *47*(4), e2019GL085987. https://doi.org/10.1029/2019GL08598

Gan, L., Li, W., Ma, Q., Artemyev, A. V., & Albert, J. M. (2020). Unraveling the formation mechanism for the bursts of electron butterfly distributions: Test particle and quasilinear simulations. *Geophysical Research Letters*, *47*(21), e2020GL090749. https://doi.org/10.1029/2020GL090749

Gannon, J. L., Li, X., & Heynderickx, D. (2007). Pitch angle distribution analysis of radiation belt electrons based on Combined Release and Radiation Effects Satellite Medium Electrons A data. *Journal of Geophysical Research*, *112*(A5), A05212. https://doi.org/10.1029/2005JA011565

Gao, X., Chen, R., Lu, Q., Chen, L., Chen, H., & Wang, X. (2022). Observational evidence for the origin of repetitive chorus emissions. *Geophysical Research Letters*, *49*(12), e2022GL099000. https://doi.org/10.1029/2022GL099000

Gao, X., Lu, Q., Kang, N., Ke, Y., Ma, J., Tsurutani, B., et al. (2022). Study on source region and generation mechanism of oblique whistler-mode waves in the Earth's magnetosphere. *Journal of Geophysical Research: Space Physics*, *127*(9), e2022JA030804. https://doi.org/10.1029/2022JA030804

Gu, X., Zhao, Z., Ni, B., Shprits, Y. Y., & Zhou, C. (2011). Statistical analysis of pitch angle distribution of radiation belt energetic electrons near the geostationary orbit: CRRES observations. *Journal of Geophysical Research*, *116*(A1), A01208. https://doi.org/10.1029/2010JA016052

Hanzelka, M., & Santolík, O. (2022). Effects of field-aligned cold plasma density filaments on the fine structure of chorus. *Geophysical Research Letters*, *49*(24), e2022GL101654. https://doi.org/10.1029/2022GL101654

Horne, R. B., Meredith, N. P., Thorne, R. M., Heynderickx, D., Iles, R. H. A., & Anderson, R. R. (2003). Evolution of energetic electron pitch angle distributions during storm time electron acceleration to megaelectronvolt energies. *Journal of Geophysical Research*, *108*(A1), 1016. https://doi.org/10.1029/2001JA009165

Horne, R. B., Thorne, R. M., Glauert, S. A., Meredith, N. P., Pokhotelov, D., & Santolik, O. (2007). Electron acceleration in the Van Allen radiation belts by fast magnetosonic waves. *Geophysical Research Letters*, *34*(17), L17107. https://doi.org/10.1029/2007GL030267

Hosseini, P., Agapitov, O., Harid, V., & Gołkowski, M. (2021). Evidence of small scale plasma irregularity effects on whistler mode chorus propagation. *Geophysical Research Letters*, *48*(5), e92850. https://doi.org/10.1029/2021GL092850

Hua, M., Ni, B., Li, W., Gu, X., Fu, S., Shi, R., et al. (2019). Evolution of radiation belt electron pitch angle distribution due to combined scattering by plasmaspheric hiss and magnetosonic waves. *Geophysical Research Letters*, *46*(6), 3033–3042. https://doi.org/10.1029/2018GL081828

Katoh, Y. (2014). A simulation study of the propagation of whistler-mode chorus in the Earth's inner magnetosphere. *Earth Planets and Space*, *66*(1), 1–12. https://doi.org/10.1186/1880-5981-66-6

Ke, Y., Chen, L., Gao, X., Lu, Q., Wang, X., Chen, R., et al. (2021). Whistler-mode waves trapped by density irregularities in the Earth's magnetosphere. *Geophysical Research Letters*, *48*(7), e2020GL092305. https://doi.org/10.1029/2020GL092305

Ke, Y., Gao, X., Lu, Q., Wang, X., & Chen, R. (2024). Simulation dataset of "Butterfly distributions of energetic electrons driven by ducted and nonducted chorus waves" [Dataset]. *Zenodo*. https://doi.org/10.5281/zenodo.10494935

Ke, Y., Gao, X., Lu, Q., Wang, X., Chen, R., Chen, H., & Wang, S. (2022). Deformation of electron distributions due to Landau trapping by the whistler-mode wave. *Geophysical Research Letters*, *49*(3), e2021GL096428. https://doi.org/10.1029/2021GL096428

Ke, Y., Lu, Q., Gao, X., Chen, H., & Chen, R. (2022). Ray-tracing simulations of whistler-mode wave propagation in different rescaled dipole magnetic fields. *Earth Planetary Physics.*, *6*(6), 555–562. https://doi.org/10.26464/epp2022048

Kurita, S., Miyoshi, Y., Kasahara, S., Yokota, S., Kasahara, Y., Matsuda, S., et al. (2018). Deformation of electron pitch angle distributions caused by upper band chorus observed by the Arase satellite. *Geophysical Research Letters*, *45*(16), 7996–8004. https://doi.org/10.1029/2018GL079104

LeDocq, M. J., Gurnett, D. A., & Hospodarsky, G. B. (1998). Chorus source locations from VLF poynting flux measurements with the polar spacecraft. *Geophysical Research Letters*, *25*(21), 4063–4066. https://doi.org/10.1029/1998GL900071

Li, J., Ni, B., Ma, Q., Xie, L., Pu, Z., Fu, S., et al. (2016). Formation of energetic electron butterfly distributions by magnetosonic waves via Landau resonance. *Geophysical Research Letters*, *43*(7), 3009–3016. https://doi.org/10.1002/2016GL067853

Li, J., Ni, B., Xie, L., Pu, Z., Bortnik, J., Thorne, R. M., et al. (2014). Interactions between magnetosonic waves and radiation belt electrons: Comparisons of quasi-linear calculations with test particle simulations. *Geophysical Research Letters*, *41*(14), 4828–4834. https://doi.org/10.1002/2014GL060461

Li, W., Thorne, R. M., Angelopoulos, V., Bortnik, J., Cully, C. M., Ni, B., et al. (2009). Global distribution of whistler-mode chorus waves observed on the THEMIS spacecraft. *Geophysical Research Letters*, *36*(9), L09104. https://doi.org/10.1029/2009GL037595

Li, W., Thorne, R. M., Bortnik, J., Tao, X., & Angelopoulos, V. (2012). Characteristics of hiss-like and discrete whistler mode emissions. *Geophysical Research Letters*, *39*(18), L18106. https://doi.org/10.1029/2012GL053206

Liu, X., Gu, W., Xia, Z., Chen, L., & Horne, R. B. (2021). Frequency-dependent modulation of whistler-mode waves by density irregularities during the recovery phase of a geomagnetic storm. *Geophysical Research Letters*, *48*(16), e2021GL093095. https://doi.org/10.1029/2021GL093095

Lu, Q., Chen, L., Wang, X., Gao, X., Lin, Y., & Wang, S. (2021). Repetitive emissions of rising-tone chorus waves in the inner magnetosphere. *Geophysical Research Letters*, *48*(15), e2021GL094979. https://doi.org/10.1029/2021GL094979

Lu, Q., Ke, Y., Wang, X., Liu, K., Gao, X., Chen, L., & Wang, S. (2019). Two-dimensional general curvilinear particle-in-cell (gcPIC) simulation of rising-tone chorus waves in a dipole magnetic field. *Journal of Geophysical Research: Space Physics*, *124*(6), 4157–4167. https://doi.org/10.1029/2019JA026586

Lyons, L. R. (1977). Adiabatic evolution of trapped particle pitch angle distributions during a storm main phase. *Journal of Geophysical Research*, *82*(16), 2428–2432. https://doi.org/10.1029/JA082i016p02428

Lyons, L. R., & Williams, D. J. (1975). The quiet time structure of energetic (35–560 keV) radiation belt electrons. *Journal of Geophysical Research*, *80*(7), 943–950. https://doi.org/10.1029/JA080i007p00943

Ma, Q., Li, W., Thorne, R. M., Bortnik, J., Kletzing, C. A., Kurth, W. S., & Hospodarsky, G. B. (2015). Electron scattering by magnetosonic waves in the inner magnetosphere. *Journal of Geophysical Research: Space Physics*, *121*(1), 274–285. https://doi.org/10.1002/2015JA021992

Meredith, N. P., Horne, R. B., Johnstone, A. D., & Anderson, R. R. (2000). The temporal evolution of electron distributions and associated wave activity following substorm injections in the inner magnetosphere. *Journal of Geophysical Research*, *105*(A6), 12907–12917. https://doi.org/10.1029/2000JA900010

Meredith, N. P., Horne, R. B., Thorne, R. M., & Anderson, R. R. (2009). Survey of upper band chorus and ECH waves: Implications for the diffuse aurora. *Journal of Geophysical Research*, *114*(A7), A07218. https://doi.org/10.1029/2009JA014230

Ni, B., Hua, M., Zhou, R., Yi, J., & Fu, S. (2017). Competition between outer zone electron scattering by plasmaspheric hiss and magnetosonic waves. *Geophysical Research Letters*, *44*(8), 3465–3474. https://doi.org/10.1002/2017GL072989

Ni, B., Yan, L., Fu, S., Gu, X., Cao, X., Xiang, Z., & Zhang, Y. (2020). Distinct formation and evolution characteristics of outer radiation belt electron butterfly pitch angle distributions observed by Van Allen Probes. *Geophysical Research Letters*, *47*(4), e2019GL086487. https://doi.org/10.1029/2019GL086487

Ni, B., Zou, Z., Fu, S., Cao, X., Gu, X., & Xiang, Z. (2018). Resonant scattering of radiation belt electrons by off-equatorial magnetosonic waves. *Geophysical Research Letters*, *45*(3), 1228–1236. https://doi.org/10.1002/2017GL075788

Ni, B., Zou, Z., Gu, X., Zhou, C., Thorne, R. M., Bortnik, J., et al. (2015). Variability of the pitch angle distribution of radiation belt ultrarelativistic electrons during and following intense geomagnetic storms: Van Allen Probes observations. *Journal of Geophysical Research: Space Physics*, *120*(6), 4863–4876. https://doi.org/10.1002/2015JA021065

Ni, B., Zou, Z., Li, X., Bortnik, J., Xie, L., & Gu, X. (2016). Occurrence characteristics of outer zone relativistic electron butterfly distribution: A survey of Van Allen Probes REPT measurements. *Geophysical Research Letters*, *43*(11), 5644–5652. https://doi.org/10.1002/2016GL069350

Peng, Y., Ma, Q., Li, W., Gan, L., & Shen, X.-C. (2022). Multi-event analysis of the correlation between chorus waves and electron butterfly distribution using Van Allen Probes observation. *Journal of Geophysical Research: Space Physics*, *127*(12), e2022JA030806. https://doi.org/10.1029/2022JA030806

Saito, S., Kurita, S., Miyoshi, Y., Kasahara, S., Yokota, S., Keika, K., et al. (2021). Data-driven simulation of rapid flux enhancement of energetic electrons with an upper-band whistler burst. *Journal of Geophysical Research: Space Physics*, *126*(4), e2020JA028979. https://doi.org/10.1029/2020JA028979

Saito, S., & Miyoshi, Y. (2022). Butterfly distribution of relativistic electrons driven by parallel propagating lower band whistler chorus waves. *Geophysical Research Letters*, *49*(12), e2022GL099605. https://doi.org/10.1029/2022GL099605

Santolík, O., & Gurnett, D. A. (2003). Transverse dimensions of chorus in the source region. *Geophysical Research Letters*, *30*(2), 1031. https://doi.org/10.1029/2002GL016178

Santolík, O., Gurnett, D. A., Pickett, J. S., Parrot, M., & Cornilleau-Wehrlin, N. (2005). Central position of the source region of storm-time chorus. *Planetary and Space Science*, *53*(1–3), 299–305. https://doi.org/10.1016/j.pss.2004.09.056

Selesnick, R. S., & Blake, J. B. (2002). Relativistic electron drift shell splitting. *Journal of Geophysical Research*, *107*(A9), 1265. https://doi.org/10.1029/2001JA009179

Shen, X. C., Li, W., Ma, Q., Agapitov, O., & Nishimura, Y. (2019). Statistical analysis of transverse size of lower band chorus waves using simultaneous multisatellite observations. *Geophysical Research Letters*, *46*(11), 5725–5734. https://doi.org/10.1029/2019gl083118

Shue, J. H., Hsieh, Y.-K., Tam, S. W., Wang, K., Fu, H. S., Bortnik, J., et al. (2015). Local time distributions of repetition periods for rising tone lower band chorus waves in the magnetosphere. *Geophysical Research Letters*, *42*(20), 8294–8301. https://doi.org/10.1002/2015GL066107

Shue, J. H., Nariyuki, Y., Katoh, Y., Saito, S., Kasahara, Y., Hsieh, Y. K., et al. (2019). A systematic study in characteristics of lower band rising-tone chorus elements. *Journal of Geophysical Research: Space Physics*, *124*(11), 9003–9016. https://doi.org/10.1029/0027ja037368

Sibeck, D. G., McEntire, R. W., Lui, A. T. Y., Lopez, R. E., & Krimigis, S. M. (1987). Magnetic field drift shell splitting: Cause of unusual dayside particle pitch angle distributions during storms and substorms. *Journal of Geophysical Research*, *92*(A12), 13345–13497. https://doi.org/10.1029/ja092ia12p13485

Smith, R. L., Helliwell, R. A., & Yabroff, I. W. (1960). A theory of trapping of whistlers in field-aligned columns of enhanced ionization. *Journal of Geophysical Research*, *65*(3), 815–823. https://doi.org/10.1029/JZ065i003p00815

Streltsov, A. V., Lampe, M., Manheimer, W., Ganguli, G., & Joyce, G. (2006). Whistler propagation in inhomogeneous plasma. *Journal of Geophysical Research*, *111*(A3), A03216. https://doi.org/10.1029/2005ja011357

Su, Z., Xiao, F., Zheng, H., & Wang, S. (2010). Combined radial diffusion and adiabatic transport of radiation belt electrons with arbitrary pitch angles. *Journal of Geophysical Research*, *115*(A10), A10249. https://doi.org/10.1029/2010JA015903

Tao, X., & Bortnik, J. (2010). Nonlinear interactions between relativistic radiation belt electrons and oblique whistler mode waves. *Nonlinear Processes in Geophysics*, *17*(5), 599–604. https://doi.org/10.5194/npg-17-599-2010

Teng, S., Tao, X., & Li, W. (2019). Typical characteristics of whistler mode waves categorized by their spectral properties using Van Allen Probes observations. *Geophysical Research Letters*, *46*(7), 3607–3614. https://doi.org/10.1029/2019GL082161

Teng, S., Tao, X., Xie, Y., Zonca, F., Chen, L., Fang, W. B., & Wang, S. (2017). Analysis of the duration of rising tone chorus elements. *Geophysical Research Letters*, *44*(24), 12074–12082. https://doi.org/10.1002/2017gl075824

Tsurutani, B. T., & Smith, E. J. (1974). Postmidnight chorus: A substorm phenomenon. *Journal of Geophysical Research*, *79*(1), 118–127. https://doi.org/10.1029/JA079i001p00118

West, H. I., Jr., Buck, R. M., & Walton, J. R. (1972). Shadowing of electron azimuthal-drift motions near the noon magnetopause. *Nature; Physical Science*, *240*(97), 6–7. https://doi.org/10.1038/physci240006a0

West, H. I., Jr., Buck, R. M., & Walton, J. R. (1973). Electron pitch angle distributions throughout the magnetosphere as observed on Ogo 5. *Journal of Geophysical Research*, *78*(7), 1064–1081. https://doi.org/10.1029/ja078i007p01064

Xiao, F., Yang, C., Su, Z., Zhou, Q., He, Z., He, Y., et al. (2015). Wave-driven butterfly distribution of Van Allen belt relativistic electrons. *Nature Communications*, *6*(1), 8590. https://doi.org/10.1038/ncomms9590

Xiong, Y., Chen, L., Xie, L., Fu, S., Xia, Z., & Pu, Z. (2017). Relativistic electron's butterfly pitch angle distribution modulated by localized background magnetic field perturbation driven by hot ring current ions. *Geophysical Research Letters*, *44*(10), 4393–4400. https://doi.org/10.1002/2017GL072558

Zhao, H., Li, X., Blake, J. B., Fennell, J. F., Claudepierre, S. G., Baker, D. N., et al. (2014). Characteristics of pitch angle distributions of hundreds of keV electrons in the slot region and inner radiation belt. *Journal of Geophysical Research: Space Physics*, *119*(12), 9543–9557. https://doi.org/10.1002/2014JA020386